2D AlB_2 flakes for epitaxial thin film growth

Mohammad Humood
Department of Mechanical Engineering, Texas A&M University, College Station, Texas 77843, USA

Jacob L. Meyer
ATSP Innovations, Champaign, Illinois 61820, USA

Stanislav V. Verkhoturov
Department of Chemistry, Texas A&M University, College Station, Texas 77843, USA

Tanil Ozkan
Department of Mechanical Engineering, Texas A&M University, College Station, Texas 77843, USA

Michael Eller and Emile A. Schweikert
Department of Chemistry, Texas A&M University, College Station, Texas 77843, USA

James Economy
ATSP Innovations, Champaign, Illinois 61820, USA

Andreas A. Polycarpou[a)]
Department of Mechanical Engineering, Texas A&M University, College Station, Texas 77843, USA

(Received 16 January 2018; accepted 15 May 2018)

In this study, we report on the mechanical cleavage of conductive metal-based aluminum diboride (AlB_2) flakes. The cleavage resulted in a highly single crystalline 2D material and had an atomically flat and smooth surface as shown by atomic force microscopy (AFM) and secondary ion mass spectrometry. Nanoindentation and AFM imaging of freshly cleaved specimens revealed sub-nm roughness and 30% improvement in the nanomechanical properties as compared to the as-grown AlB_2 flakes. Once exposed to ambient air, the cleaved AlB_2 flakes formed a superficial oxidation layer of less than 1 nm thickness within 5 min. Owing to the smooth surface, ultra-thin and stable oxide layer, and the excellent mechanical and electrical characteristics of AlB_2, the cleaved flakes present an ideal 2D material for emerging applications in microfabrication such as the growth of epitaxial thin films. To prove the sub-nm surface characteristics of cleaved AlB_2, a 10-nm thick TiO_2 film was deposited on a freshly cleaved AlB_2 using atomic layer deposition. Surface roughness and compositional consistency of this film were compared with a control sample deposited on Si. The TiO_2 film on AlB_2 showed a distinct thin interface layer with fewer defects than TiO_2 on Si and superior flatness.

I. INTRODUCTION

Since the discovery of the first graphene flake in 2004 through the mechanical cleavage of highly ordered pyrolytic graphite, two-dimensional (2D) nanomaterials have attracted attention due to their potential use in a range of applications such as catalysis, electronic and optoelectronic devices, electrodes for energy storages, and nanocomposites.[1,2] 2D materials such as graphene have versatile and enhanced mechanical, chemical, and electrical properties.[3,4] The success of 2D graphene has motivated scientists in the last years to pursue the search for 3D materials that can be exfoliated by separating a 3D material into single or few 2D layers.[5] These efforts successfully have led to the discovery of promising new 2D materials beyond graphene such as hexagonal boron nitride and transition metal dichalcogenides.[6,7] Therefore, the space of 2D materials is expanding and getting more mature as a distinct class of materials bringing new capabilities, functionalities, and technologies, which were not attainable with their parent 3D materials.

Layered metal oxides, nitrides, and carbides are already being explored and were found to be promising 2D materials for different electronic devices.[8] To date, there is no literature about 2D materials based on metal borides, while there are many advantages of pursuing metal borides as 2D materials such as low temperature synthesis, especially aluminum. In addition, AlB_2 has the unique properties of boron, and more cost-effective and practical to produce than pure boron, which is similar to graphene oxide, as compared to graphene.[9] Furthermore, AlB_2 single crystals show metallic conductivity in the axis parallel to the basal hexagonal plane.[10] In terms of potential applications, AlB_2 flakes were found to be

[a)]Address all correspondence to this author.
e-mail: apolycarpou@tamu.edu
DOI: 10.1557/jmr.2018.173

 © Materials Research Society 2018

https://doi.org/10.1557/jmr.2018.173 Published online by Cambridge University Press

a very effective reinforcement for polymer composites such as epoxies, with outstanding mechanical performance.[11,12] Therefore, AlB_2 flakes can be utilized for conductive polymer composites. Due to the hexagonal structure, thermal and chemical stability, and electrical conductivity, metal borides have been used as substrates for heteroepitaxial growth of semiconductor devices.[13,14]

The hexagonal crystal structure of AlB_2 is one of the simplest inorganic structure types: a simple hexagonal cell of aluminum atoms with two boron atoms occupying the trigonal prismatic sites. The boron atoms form graphite-like sheets with the layers arranged into honeycomb-like structures separated by a lattice parameter (c) of 3.25 Å. AlB_2 is a MB_2 type material where M is for metals, and it has a metastable phase at room temperature.[15,16]

Two morphologies of AlB_2 crystallites have previously been identified—a low aspect ratio (LAR) equiaxed form of micron length, commonly used in grain refining of aluminum alloys, and a high aspect ratio (HAR) flake of up to a centimeter in width.[17–20] The growth of HAR AlB_2 single crystal flakes within an aluminum melt was demonstrated starting with a master alloy containing LAR AlB_2, which was heated above the Al–B liquidus region followed by various heat treatments.[12,21] The study by Hall and Economy showed that HAR flakes could be synthesized by heating merely above the $Al_{(L)} + AlB_{12} \leftrightarrow AlB_2$ peritectic transition temperature, which is permitted by the lengthy growth time of AlB_{12} from the Al–B melt.[22] In addition, aluminothermic processes have also been used to synthesize HAR AlB_2 flakes.[23]

There are significant advantages of achieving a smoother substrate with less surface features/defects in order to grow high quality epitaxial thin films. First, a uniform growth of thin films demands substrates that have both smooth and flat surfaces at the atomic level to avoid inhomogeneous nucleation and growth of the film. A rough surface can result in film growth with islands especially as the thickness of the deposited film is reduced. Moreover, the surface roughness is a key factor for the oxidation kinetics since oxidation proceeds in a layer-by-layer manner. Therefore, reducing surface heights and defects will reduce the thickness of the surface oxide layer achieving a thin complete oxide layer. Typically, polishing processes such as chemical–mechanical polishing are used to smoothen the surface roughness of the substrate. This was successfully achieved herein using the mechanical cleavage of the substrate without the need for any extra polishing or etching of the substrate's surface, which simplified the synthesis process of the TiO_2 film. Once this atomically flat surface is achieved using cleavage, its stability against oxidation and surface reconstruction over short time in air is another critical requirement.[24] Rapid oxidation after cleavage can result in the roughening of surface.[25] Therefore, a low oxidation degree of the substrate is favorable for epitaxial thin film growth.

In this work, we show that millimeter-scale HAR AlB_2 crystals grown in situ in an aluminum melt are cleavable via dry mechanical exfoliation resulting in 2D AlB_2.[26–28] This is of interest to investigations toward low-dimensional boron phases,[29–31] as a surface for epitaxial growth experiments, and the relatively high p-type conductivity (7.5 μΩ cm) of the AlB_2 phase in the basal plane.[16] We monitored the surface of cleaved AlB_2 in terms of roughness and oxidation using atomic force microscopy (AFM) and secondary ion mass spectrometry (SIMS), respectively. The 2D cleaved flakes were found to be stable under ambient conditions for sufficient time to carry out the subsequent thin film growth of TiO_2 using atomic layer deposition (ALD).

II. EXPERIMENTAL DETAILS

A. Fabrication of HAR flakes

Initially, an aluminum–boron (5 wt%) master alloy (KB Alloys, Wayne Pennsylvania) was alloyed with a 99.99% pure aluminum ingot (Alcoa, Pittsburgh, Pennsylvania) by heating to 750 °C in an alumina crucible under flowing argon atmosphere and then cast in a cylindrical graphite mold. To produce the HAR flakes in an aluminum solution, a cast ingot was then heated to 1360 °C (above liquidus temperature) under flowing argon in an alumina crucible and then cooled to 900 °C (below peritectic temperature) for one hour after which the sample was allowed to cool to room temperature at a rate of 0.2 °C/min. HAR AlB_2 flakes were then extracted by etching away the aluminum matrix by 37% hydrochloric acid (Fisher Scientific, Waltham, Massachusetts), which yielded aluminum chloride ($AlCl_3$) precipitates and hydrogen gas. HAR AlB_2 flakes were separated from the liquid phase by vacuum filtration using a Büchner funnel (Sigma Aldrich, St. Louis, Missouri). Wet residue, composed of aluminum chloride powder and HAR AlB_2 flakes, was then washed with copious deionized water followed by isopropanol and dried in a convection oven at 110 °C. The as-grown flakes were then separated from the powder by gentle sieving by hand with a 90 μm mesh sieve. This was followed by gentle flush with isopropanol and subsequent drying at 110 °C for 2 h. The as-grown flakes did not form an oxide layer during synthesis because they were protected from oxygen by the argon atmosphere, and more importantly by the aluminum melt. The native oxide formed during and after the extraction and drying process from exposure to atmospheric oxygen rather than the free oxygen in the aluminum melt.

B. AFM

The AFM images were scanned using a Cypher AFM instrument (Asylum Research, Santa Barbara, California). The scans were carried out in the noncontact mode

https://doi.org/10.1557/jmr.2018.173 Published online by Cambridge University Press

and with an 8 nm diameter silicon tip, and a scan rate of 0.5 Hz and 512 samples per line.

C. Nanoindentation

The mechanical properties were measured using a commercial indenter, TI Premier (Bruker, Minneapolis, Minnesota), and the experiments were carried out using load-control mode. A cube corner probe was used (tip radius of 40 nm) to maintain shallow indentation depths. For all experiments, 5 s time periods for loading and unloading and 2 s dwell time at maximum nanoindentation load were used. The hardness (H) and reduced elastic modulus (E_r) were obtained from the first one-third of the unloading curve according to the Oliver and Pharr method.[29] The indenter probe was calibrated using a standard fused quartz sample.

D. X-ray diffraction

A Siemens/Bruker (Madison, Wisconsin) D-5000 X-ray diffraction (XRD) system (Radiation is Cu K_α and wavelength is 0.15418 nm) is used to obtain crystallographic structure determination.

E. SIMS

A CAMECA 4f SIMS (Madison, Wisconsin) was used in the dynamic mode, for the measurement of the thickness of the oxide layers. The profiling was done with 14.5 keV Cs^+ ion beam (raster 500 × 500 μm^2, image collimation diameter 50 μm, and sputtering rate 0.01 nm/s).

F. ALD

An Ultratech/Cambridge NanoTech, Savannah S200 ALD system (Waltham, Massachusetts) is used to deposit TiO_2. ALD allows atomic-level control for the growth, which results in an epitaxial growth of the film.

III. RESULTS AND DISCUSSION

A. Nanomechanical properties

The as-grown flakes were secured on AFM metal disks using an adhesive and left to dry overnight in a well-ventilated room. Mechanical cleavage was then performed using mechanical exfoliation (3 M scotch tape) inside a glove box filled with argon gas. The scotch tape was pressed on the flake and gently peeled up. This exposed the ultra-smooth pristine interior with an extremely flat surface. Figures 1(a) and 1(b) show SEM cross-sectional views of both the as-grown and cleaved flakes. The thicknesses were 6 and 10 μm for cleaved and as-grown flakes, respectively. The mechanical cleavage removed about 4 μm thick layer of the as-grown flake and was facilitated by the Kirkendall void formed due to diffusion rate differences and compositional gradients encountered during the synthesis of AlB_2 flakes. The cross-sectional SEM image in Fig. 1(a) shows the length scale and orientation of these voids pointing to morphological origins of the flake formation above the liquidus temperature. Similar Kirkendall voids were observed with other binary alloy systems of Al, specifically Ti–Al and Ni–Al systems.[32] However, to the best of our knowledge, this is the first scientific study reporting the presence of planar Kirkendall voids in AlB_2 flakes.

Figure 2(a) shows a step between the surfaces of the as-grown and cleaved flakes. Figure 2(c) shows the cleaved surface over a large area (10,000 × 10,000 Å) with an R_q roughness of 1.07 Å and a z-height noise floor of 0.5 Å. The unit cell, c_o, is found to be 3.01 Å. The cleaved flake has 80 times lower R_q roughness than the as-grown flake, which has significant defects and intermetallic formations [see Fig. 2(b)].

The nanoindentation probe was calibrated according to the Oliver–Pharr method between contact depths of 3–65 nm.[33] Figure 3(a) shows the residual image of a 150 μN peak load indentation, measured on the cleaved surface. The cross-sectional profile shows atomic-scale topography in Fig. 3(a), where 3 Å height accounts for an atomic step height. There is no clear pile-up under this indentation load. For a higher indentation load of 720 μN, Fig. 3(b) illustrates a significant pile-up around the indentation mark. The pile-up phenomenon shows highly crystallographic localized material flow.[34]

Table I provides the extracted nanomechanical properties of both samples: as-grown AlB_2 and cleaved AlB_2 flakes. The cleaved sample had higher elastic modulus and hardness. The reduced elastic modulus value (~174 GPa) was close to the bulk modulus measurement available both as a simulated/calculated value provided by Duan et al.,[35] Shein and Ivanovskii,[36] and Gaillac et al.[37] Figures 4(a) and 4(b) show representative load/displacement curves for both samples for indentation loads of 150 and 720 μN, respectively. There were discrete fracture events in both samples, being more pronounced in the cleaved sample. The first fracture event in the cleaved sample took place in depths of 3–5 nm where the tip broke through a specific number of layers, where c = 3.25 Å. Therefore, for such nanoindentation depths, it was about 10–15 layers. These pop-in events in the loading part of the load–displacement curve of the cleaved sample were attributed to transverse cracking due to relatively lower incompressibility of AlB_2 on the plane of hexagonal symmetry.[21] This response is further amplified by the high Zener anisotropy as shown through first-principles calculations.[35] Through the introduction of the freshly cleaved surface, we eliminated the inherent structural compliance of the flake originating from the Kirkendall void, which clearly manifested itself through the increase in reduced modulus, summarized in Table I.

The freshly cleaved AlB_2 exhibits a harder and more brittle response. This experimental observation is in agreement with the findings of the first-principles

https://doi.org/10.1557/jmr.2018.173 Published online by Cambridge University Press

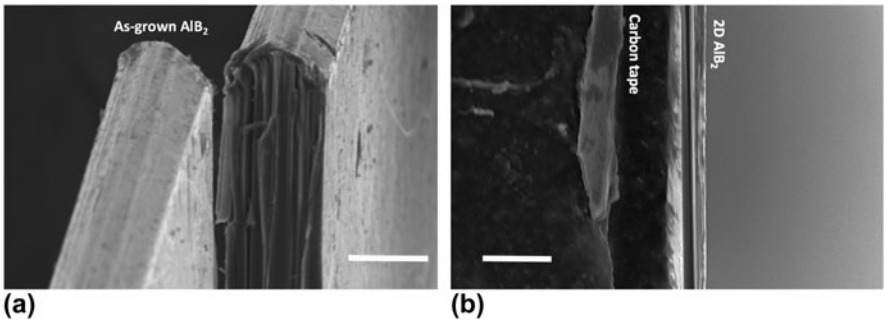


FIG. 1. Cross-sectional SEM images for the (a) as-grown and (b) cleaved AlB_2 surfaces. Scale bar is 10 μm.

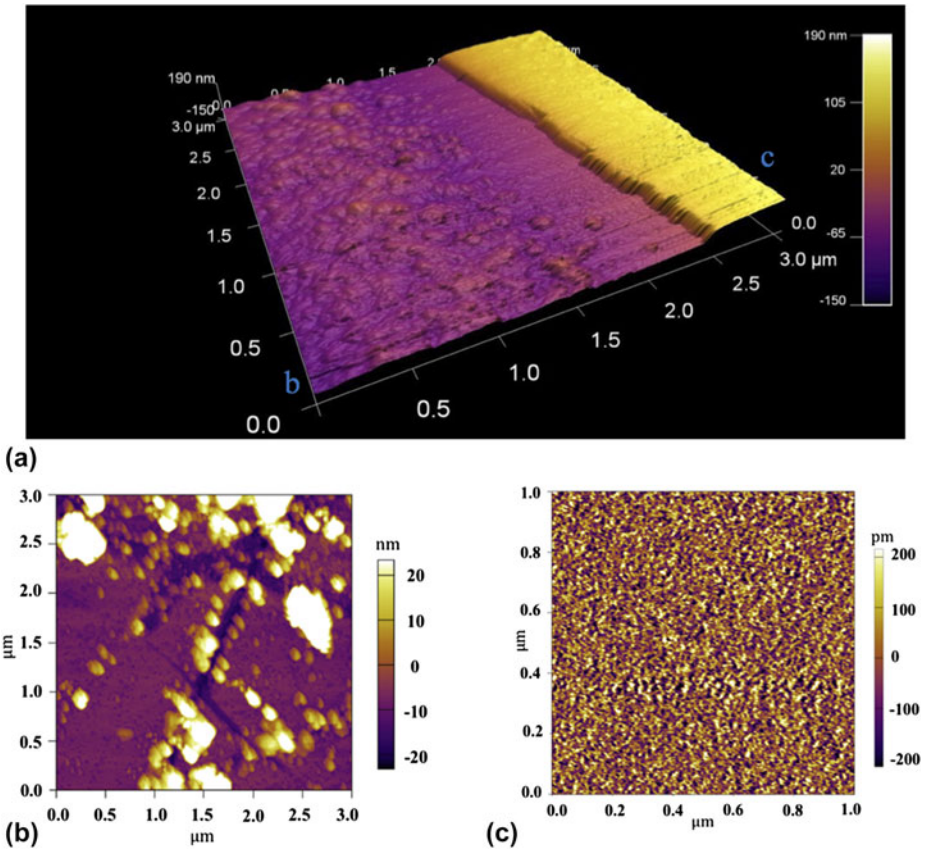


FIG. 2. (a) AFM of the AlB_2 flake showing a step generated after cleavage, (b) as-grown, and (c) cleaved surfaces.

calculation study, which assigned the highest brittleness among all metal diborides to AlB_2, based on the bulk to shear moduli ratio.[35] The lack of structural compliance due to the removal of the Kirkendall void combined with the intrinsically higher incompressibility of AlB_2 normal to the hexagonal symmetry plane explains the hardness increase with the freshly cleaved samples.

In the case of as-grown flakes, there is a thick superficial oxide layer, which provides a compliant response for penetration depths less than 10 nm. For the same sample, the lower frequency of fracture events, even at higher loads, points to a more uniform distribution of applied stress into the underlying AlB_2 through the conformal oxide. A further insight concerning the native oxide is provided using SIMS depth profiling. This surface layer was determined to be a conformal oxide consisting of Al_2O_3 and B_2O_3.

B. Surface chemistry of cleaved AlB_2

1. XRD

Figure 5(a) presents the XRD patterns obtained over the as-grown and cleaved AlB_2 flakes. Figure 5(b) shows more single-crystalline surface for the cleaved flake, as

https://doi.org/10.1557/jmr.2018.173 Published online by Cambridge University Press

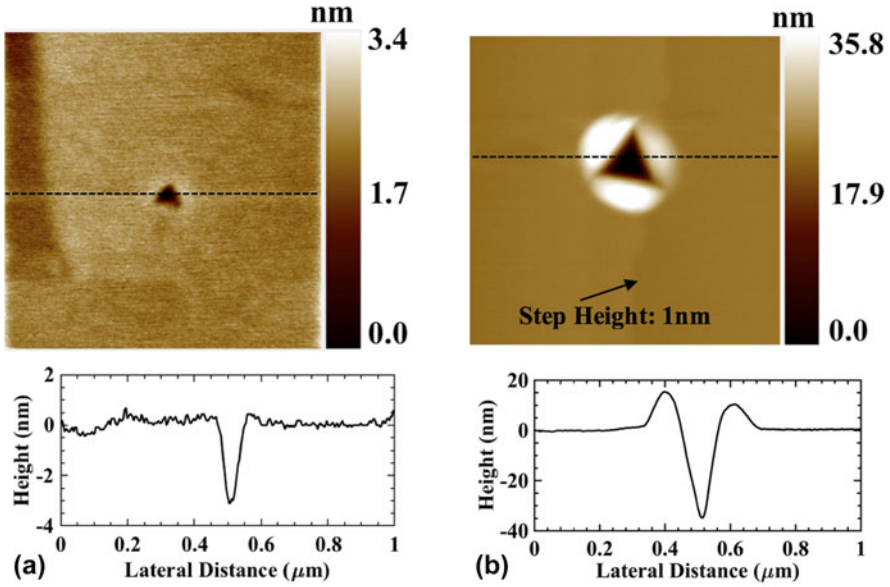


FIG. 3. Residual indentation images and cross-section profiles (1 × 1 μm) after (a) 150 μN and (b) 720 μN indentation load on the cleaved sample under ambient dry conditions.

TABLE I. Nanomechanical properties of the as-grown and cleaved AlB_2 flakes.

Specimen	E_r (GPa)	H (GPa)	R_q (Å)
AlB_2 as-grown	174.36 ± 8.33	22.00 ± 2.16	81.1
AlB_2 cleaved	183.92 ± 9.00	28.72 ± 1.99	1.1

shown by the sharper peak. Figure 5(c) shows a semilog scale for the cleaved surface with different crystallographic planes, which are labeled in the figure. The dashed lines represent the relative normalized polycrystalline peak intensities of AlB_2, which are extracted from the literature.[38] The cleaved plane showed only the diffraction peaks corresponding to the basal plane.

2. SIMS depth profiling

The oxidation of AlB_2 via exposure in dry air or oxygen was investigated for the samples with main attention on the kinetics of oxidation and its growth rate. For the case of air exposure of the cleaved surface of the AlB_2 monocrystal, there is an important question concerning the oxide layers, that is, how does the few nm thickness of the oxide layer change with the time of oxidation? The kinetics of the oxidation growth rate is important to ensure the stability of the cleaved surface before the successive chemistry on the surface, such as the deposition of epitaxial thin films.

To gain further insight about the compositional analysis of AlB_2 flakes as a function of depth, SIMS CAMECA 4F was used for depth profiling. The angle of incidence of the beam was 26°. The measured secondary ions were negatively charged. Three different areas of each sample were probed. The profiles for these areas were very similar and are shown in Fig. 6. The SIMS characterization included both the as-grown and cleaved flakes. The purpose of characterizing the as-grown flake was to show the effect of cleavage on the surface roughness and oxidation.

Within the first 35 s of profiling the as-grown AlB_2 sample shown in Fig. 6(a), the surface contamination was removed (Zone I). The transition zone, Zone II, was characterized by increasing the concentration of Cs (delivered from the beam), which increased the ionization probability of the emitted ions. It means that increasing of the signals of ions in this zone did not match with the increasing concentration of the corresponding oxides. Zone III showed decreasing concentration of oxides, with increasing B and Al. The next zone was the profiling of the bare AlB_2 (the signals of B and Al are steady).

The observed high signals of AlO_2 and BO_2 indicated strong oxidation, thus the topmost layer likely consisted of oxidation states for Al and B such as Al_2O_3 and B_2O_3. Previously, the oxidation kinetics of AlB_2 were investigated for the powders which were heated in air (10° C/min).[39] It was found that at temperatures >600 °C, the oxide products Al_2O_3 and B_2O_3 form $Al_4B_2O_9$ ($2Al_2O_3{\cdot}B_2O_3$) due to strong removal of B_2O_3. For the case presented in this work, the temperature of drying in air was 110 °C only, thus likely, the products of oxidation Al_2O_3 and B_2O_3 form $Al_2O_3{\cdot}2B_2O_3$. Referring to Fig. 6, the top x-coordinate shows the profiling depth, which is calculated with the TRIM code, commonly used for sputtering (http://www.srim.org/). The profile shows that the native oxide layer was grown via exposure to

https://doi.org/10.1557/jmr.2018.173 Published online by Cambridge University Press

atmospheric oxygen during the drying of the manufactured sample, which was inserted into a convection oven at 110 °C for 120 min. The depth profile showed that the thickness of the oxide layer was ~8 nm. An interesting feature was the observation of the signal of BH. This signal was notable even at a depth of ~15 nm in the AlB_2 flake. It is likely that hydrogenation occurred at the time of synthesis of AlB_2.

Next we consider the cleaved 2D AlB_2 flake, which was exposed in air for 5 min after the mechanical cleavage. The profile of this sample was different. Within the first 40 s of profiling the cleaved sample shown in

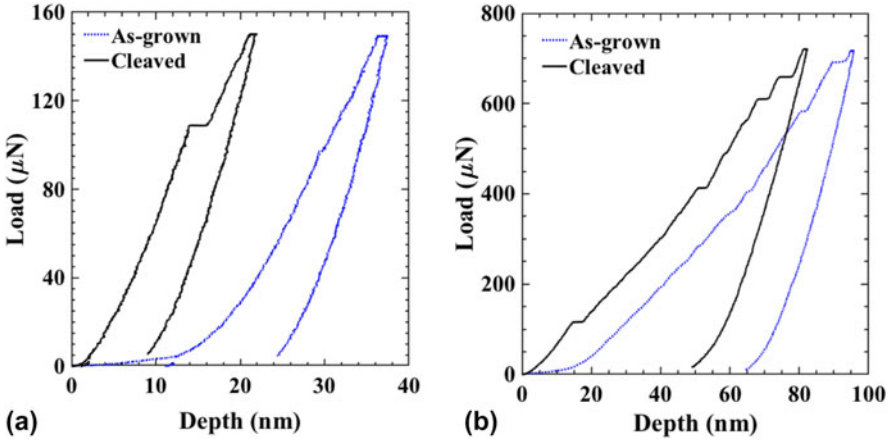


FIG. 4. Representative load–displacement curves for peak indentation loads of (a) 150 μN and (b) 720 μN, for the as-grown and cleaved samples.

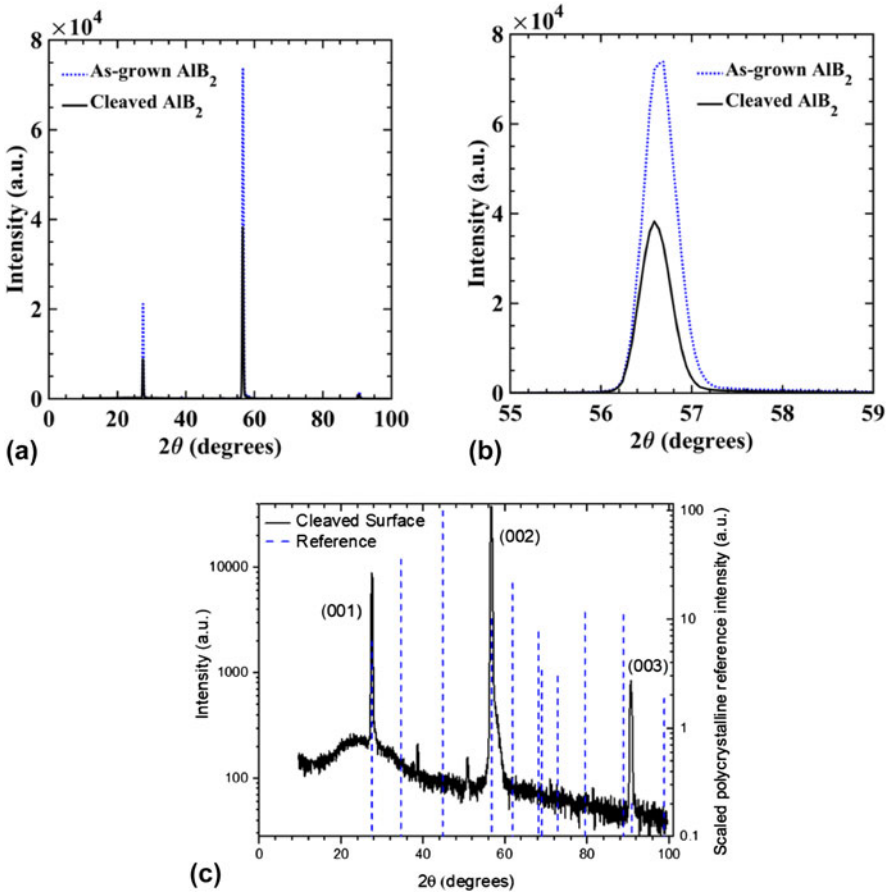


FIG. 5. XRD for the as-grown and cleaved AlB_2 flakes in (a and b) linear scale, and (c) log scale for the cleaved sample.

https://doi.org/10.1557/jmr.2018.173 Published online by Cambridge University Press

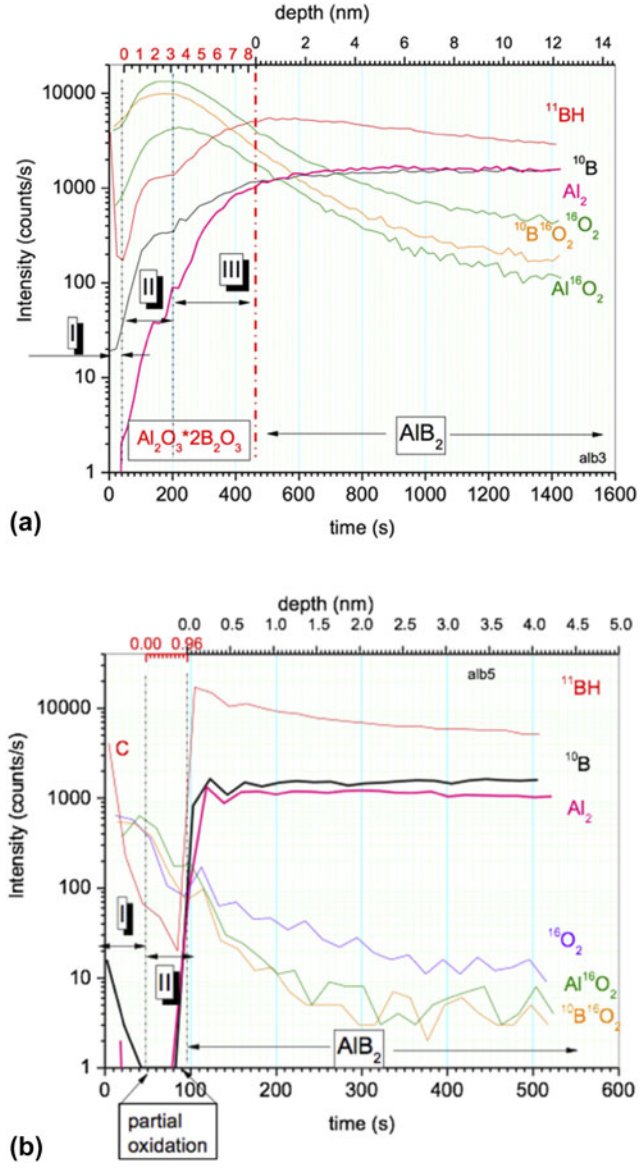


FIG. 6. Quantitative SIMS depth profiles of (a) as-grown AlB_2 and (b) cleaved AlB_2 flakes.

Fig. 6(b), the surface contamination (carbon, "natural boron") was removed (Zone I). Zone II showed the decreasing concentration of oxides, with increasing B and Al. The next zone was the profiling of the bare AlB_2 (the signals of B and Al are steady). The observed signals of AlO_2 and BO_2 indicated that the topmost molecular layer consisted of Al_2O_3 and B_2O_3 similar to the as-grown flake before the cleavage. However, the rapid decreasing of the signals of AlO_2 and BO_2 (~5 times within 1 nm of profiling) showed that the degree of oxidation was reduced with the depth. The total thickness of the oxide layer was less than 1 nm [Fig. 6(b)]. One should note that the extended low intensity signals of Al_2O_3 and B_2O_3 (intensities decrease 100 times) at the depth >2 nm were due to the common diffusion effect stimulated by the beam of primary ions of 14.5 keV Cs^+. Similar to the sample with a native oxide layer, an interesting feature was the observation of the signal of BH. This signal was notable even at a depth of ~5 nm in the AlB_2 flake. The sudden increase of signals of Al_2 and ^{10}B showed that the surface was very flat at the probing area which is of 500 × 500 μm^2. Therefore, the results of SIMS depth profiling support the findings of AFM roughness imaging.

C. Epitaxial thin film growth

To demonstrate the superior surface of cleaved AlB_2, ALD was used to deposit a TiO_2 film with a thickness of 10 nm. Also, silicon on insulator (SOI) is used for TiO_2 deposition, for comparison. Silicon is a common substrate for the growth of epitaxial thin films especially in semiconductor manufacturing. SOI refers to a layered structure of the thin silicon film (~200 nm), top of the insulator (1000 nm thick SiO_2 layer), and finally the micro-thick Si wafer substrate. The Si wafer was cleaned with acetone and methanol successively using an ultrasonic cleaner. Hot air was used to dry the Si between both solutions. The silicon was used for deposition without any further etching of the native SiO_2 oxide. The aim of this experiment was to understand how the superficial oxide layer of cleaved 2D AlB_2 and Si would influence the growth of an epitaxial thin film.

To evaluate the quality of the epitaxial growth of the TiO_2 film on both AlB_2 and Si, SIMS depth profiling and AFM topography imaging were used, as shown in Figs. 7 and 8, respectively. SIMS showed four distinct layers for the TiO_2/Si sample, where two of them were titanium oxide layers. The first layer (area I) was the pure TiO_2 film, while the second layer (area II) consisted of titanium oxide with a strong content of the carbon (perhaps hydrocarbons). The third layer was the silicon oxide with a strong content of the carbon as well. The fourth layer (area IV) is the pure Si film. The estimated thicknesses of the layers are presented as the X coordinate at the top of the graph. On the other hand, three notable profile areas were observed for the TiO_2/AlB_2 sample. Area I showed the TiO_2 layer of thickness ~9 nm. The second area was the thin natural oxide layer of AlB_2 with a thickness of ~3.7 nm. Area III was the body of the AlB_2 substrate. The AFM images were used to measure the R_q roughness (see Fig. 8). The roughness was 2.6 and 5.4 Å for the TiO_2 thin film on both AlB_2 and Si substrates, respectively. The TiO_2 thin film grown on AlB_2 was smoother as compared to the one grown on silicon. This was due to two reasons: (i) the cleaved AlB_2 had smaller surface roughness than Si and (ii) cleavage removed the majority of AlB_2 surface defects. Therefore, cleavage improved the conditions of the AlB_2 surface for epitaxial thin film growth.

https://doi.org/10.1557/jmr.2018.173 Published online by Cambridge University Press

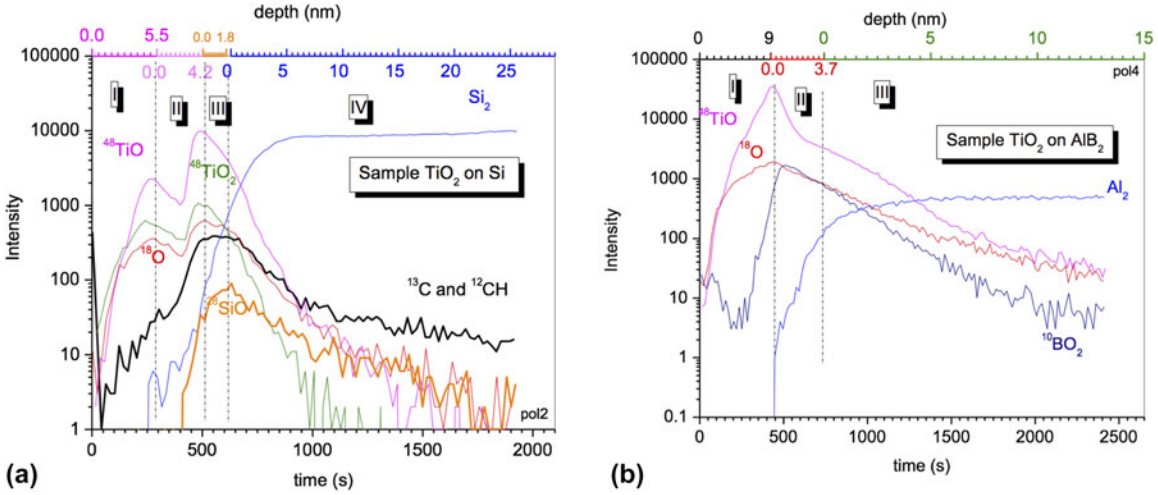


FIG. 7. Quantitative SIMS depth profile and AFM roughness images of epitaxial grown (a) TiO_2/Si and (b) TiO_2/cleaved AlB_2.

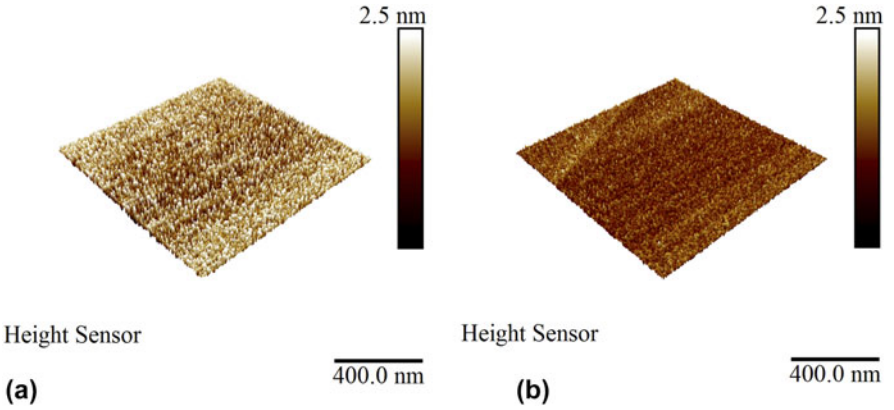


FIG. 8. AFM roughness images of the TiO_2 film deposited on the (a) silicon substrate and (b) cleaved AlB_2 surface.

IV. CONCLUSION

To achieve the growth of high-quality epitaxial thin films, the substrate needs to be smooth and flat at the atomic level, highly single crystalline, and has a stable and low degree of oxidation. The cleaved AlB_2 was found to successfully attain these requirements. The as-grown AlB_2 flake had substantial defects and evidence of intermetallic formation. The cleavage of the AlB_2 flake yielded the surface layer more single crystalline. In addition, the cleaved AlB_2 flakes had a surface roughness that was lower than the lattice parameter c of the AlB_2 phase and showed enhanced mechanical properties. Using SIMS, we were able to characterize the oxide surface and subsurface of AlB_2 at the nanoscale. The as-grown flake had a native oxide layer with a thickness of ~8 nm. This oxide layer consisted of Al_2O_3 and B_2O_3. The cleavage resulted on a 2D AlB_2 with a superficial oxide layer with an average thickness of ~1 nm. The oxide layer was stable after cleavage as shown by AFM and SIMS, providing sufficient time to carry out thin film deposition, taking advantage of the atomic-scale ultra-smooth and flat surface. TiO_2 thin film deposition showed that the cleaved AlB_2 can be a promising 2D material for thin film epitaxial growth.

ACKNOWLEDGMENTS

The authors acknowledge the use of the Materials Characterization Facility (MCF) at Texas A&M University and the Frederick Seitz Materials Research Laboratory (MRL) at the University of Illinois at Urbana–Champaign. The authors acknowledge the help of Mete Bakir in the XRD characterization of the flakes. Part of this study was funded by NSF Grant No. CHE-1308312.

REFERENCES

1. K.S. Novoselov, A.K. Geim, S.V. Morozov, D. Jiang, Y. Zhang, S.V. Dubonos, I.V. Grigorieva, and A.A. Firsov: Electric field effect in atomically thin carbon films. *Science* **306**, 666 (2004).
2. K.S. Novoselov, D. Jiang, F. Schedin, T.J. Booth, V.V. Khotkevich, S.V. Morozov, and A.K. Geim: Two-dimensional atomic crystals. *Proc. Natl. Acad. Sci. U. S. A.* **102**, 10451 (2005).

https://doi.org/10.1557/jmr.2018.173 Published online by Cambridge University Press

3. W.Y. Pan, Q.W. Bao, Y.J. Mao, B.H. Liu, and Z.P. Li: Low-temperature synthesis of nanosized metal borides through reaction of lithium borohydride with metal hydroxides or oxides. *J. Alloys Compd.* **651**, 666 (2015).
4. X. Sun, X. Liu, J. Yin, J. Yu, Y. Li, Y. Hang, X. Zhou, M. Yu, J. Li, G. Tai, and W. Guo: Two-dimensional boron crystals: Structural stability, tunable properties, fabrications and applications. *Adv. Funct. Mater.* **27**, 1603300 (2017).
5. N. Mounet, M. Gibertini, P. Schwaller, D. Campi, A. Merkys, A. Marrazzo, T. Sohier, I.E. Castelli, A. Cepellotti, G. Pizzi, and N. Marzari: Two-dimensional materials from high-throughput computational exfoliation of experimentally known compounds. *Nat. Nanotechnol.* **13**, 246 (2018).
6. A. Marrazzo, M. Gibertini, D. Campi, N. Mounet, and N. Marzari: Prediction of a large-gap and switchable kane-mele quantum spin hall insulator. *Phys. Rev. Lett.* **120**, 117701 (2018).
7. D. Pacilé, J.C. Meyer, Ç.Ö. Girit, and A. Zettl: The two-dimensional phase of boron nitride: Few-atomic-layer sheets and suspended membranes. *Appl. Phys. Lett.* **92**, 133107 (2008).
8. A. Gupta, T. Sakthivel, and S. Seal: Recent development in 2D materials beyond graphene. *Prog. Mater. Sci.* **73**, 44 (2015).
9. S. Thakur and N. Karak: Alternative methods and nature-based reagents for the reduction of graphene oxide: A review. *Carbon* **94**, 224 (2015).
10. U. Burkhardt, V. Gurin, F. Haarmann, H. Borrmann, W. Schnelle, A. Yaresko, and Y. Grin: On the electronic and structural properties of aluminum diboride $Al_{0.9}B_2$. *J. Solid State Chem.* **177**, 389 (2004).
11. Ö. Savaş and R. Kayikci: Production and wear properties of metal matrix composites reinforced with boride particles. *Mater. Des.* **51**, 641 (2013).
12. C. Deppisch, G. Liu, A. Hall, Y. Xu, A. Zangvil, J.K. Shang, and J. Economy: The crystallization and growth of AlB_2 single crystal flakes in aluminum. *J. Mater. Res.* **13**, 3485 (1998).
13. J. Suda and H. Matsunami: Heteroepitaxial growth of group-III nitrides on lattice-matched metal boride ZrB_2 (0 0 0 1) by molecular beam epitaxy. *J. Cryst. Growth* **237–239**, 1114 (2002).
14. Y. Yamada-Takamura, Z.T. Wang, Y. Fujikawa, T. Sakurai, Q.K. Xue, J. Tolle, P-L. Liu, A.V.G. Chizmeshya, J. Kouvetakis, and I.S.T. Tsong: Surface and interface studies of GaN epitaxy on Si(111) via ZrB_2 buffer layers. *Phys. Rev. Lett.* **95**, 266105 (2005).
15. R-D. Hoffmann and R. Pöttgen: AlB2-related intermetallic compounds – a comprehensive view based on group-subgroup relations. *Z. Kristallogr.–Cryst. Mater.* **216**, 127 (2001).
16. I. Loa, K. Kunc, K. Syassen, and P. Bouvier: Crystal structure and lattice dynamics of AlB_2 under pressure and implications for MgB_2. *Phys. Rev. B* **66**, 134101 (2002).
17. V.I. Matkovich, J. Economy, and R.F. Giese: Presence of carbon in aluminum borides. *J. Am. Chem. Soc.* **86**, 2337 (1964).
18. P.S. Kisly, T.A. Prikhna, and L.S. Golubyak: Properties of high-temperature solution-grown aluminium borides. *J. Less-Common Met.* **117**, 349 (1986).
19. G.V. Samsonov, V.A. Neronov, and L.K. Lamikhov: The conditions, structure and some properties of phases in the Al–B system. *J. Less-Common Met.* **67**, 291 (1979).
20. V.T. Serebryanskii and V.A. Epel'baum: Phase diagram of the aluminum–boron system. *J. Struct. Chem.* **2**, 692 (1961).
21. C. Deppisch, G. Liu, J.K. Shang, and J. Economy: Processing and mechanical properties of AlB_2 flake reinforced Al-alloy composites. *Mater. Sci. Eng. A* **225**, 153 (1997).
22. A. Hall and J. Economy: The $Al_{(L)} + AlB_{12} \leftrightarrow AlB_2$ peritectic transformation and its role in the formation of high aspect ratio AlB_2 flakes. *J. Phase Equilib.* **21**, 63 (2000).
23. A.C. Hall and J. Economy: Preparing high- and low-aspect ratio AlB_2 flakes from borax or boron oxide. *JOM* **52**, 42 (2000).
24. P.D. Padova, C. Ottaviani, C. Quaresima, B. Olivieri, P. Imperatori, E. Salomon, T. Angot, L. Quagliano, C. Romano, A. Vona, M. Muniz-Miranda, A. Generosi, B. Paci, and G.L. Lay: 24 h stability of thick multilayer silicene in air. *2D Mater.* **1**, 21003 (2014).
25. K. Ohsawa, Y. Hayashi, R. Hasunuma, and K. Yamabe: Roughness increase on surface and interface of SiO_2 grown on atomically flat Si(111) terrace. *J. Phys.: Conf. Ser.* **191**, 12031 (2009).
26. J. Kim, F. Kim, and J. Huang: Seeing graphene-based sheets. *Mater. Today* **13**, 28 (2010).
27. J. Zhu: Graphene production: New solutions to a new problem. *Nat. Nanotechnol.* **3**, 528 (2008).
28. H. Li, G. Lu, Y. Wang, Z. Yin, C. Cong, Q. He, L. Wang, F. Ding, T. Yu, and H. Zhang: Mechanical exfoliation and characterization of single-and few-layer nanosheets of WSe_2, TaS_2, and $TaSe_2$. *Small* **9**, 1974 (2013).
29. A.J. Mannix, X-F. Zhou, B. Kiraly, J.D. Wood, D. Alducin, B.D. Myers, X. Liu, B.L. Fisher, U. Santiago, J.R. Guest, M.J. Yacaman, A. Ponce, A.R. Oganov, M.C. Hersam, and N.P. Guisinger: Synthesis of borophenes: Anisotropic, two-dimensional boron polymorphs. *Science* **350**, 1513 (2015).
30. Z. Zhang, A.J. Mannix, Z. Hu, B. Kiraly, N.P. Guisinger, M.C. Hersam, and B.I. Yakobson: Substrate-induced nanoscale undulations of borophene on silver. *Nano Lett.* **16**, 6622 (2016).
31. B. Feng, J. Zhang, Q. Zhong, W. Li, S. Li, H. Li, P. Cheng, S. Meng, L. Chen, and K. Wu: Experimental realization of two-dimensional boron sheets. *Nat. Chem.* **8**, 563 (2016).
32. A. Paul, M.J.H. van Dal, A.A. Kodentsov, and F.J.J. van Loo: The kirkendall effect in multiphase diffusion. *Acta Mater.* **52**, 623 (2004).
33. W.C. Oliver and G.M. Pharr: An improved technique for determining hardness and elastic modulus using load and displacement sensing indentation experiments. *J. Mater. Res.* **7**, 1564 (1992).
34. Y. Wang, D. Raabe, C. Klüber, and F. Roters: Orientation dependence of nanoindentation pile-up patterns and of nanoindentation microtextures in copper single crystals. *Acta Mater.* **52**, 2229 (2004).
35. Y.H. Duan, Y. Sun, Z.Z. Guo, M.J. Peng, P.X. Zhu, and J.H. He: Elastic constants of AlB_2-type compounds from first-principles calculations. *Comput. Mater. Sci.* **51**, 112 (2012).
36. I.R. Shein and A.L. Ivanovskii: Elastic properties of mono- and polycrystalline hexagonal AlB_2-like diborides of *s*, *p*, and *d* metals from first-principles calculations. *J. Phys.: Condens. Matter* **20**, 415218 (2008).
37. R. Gaillac, P. Pullumbi, and F-X. Coudert: ELATE: An open-source online application for analysis and visualization of elastic tensors. *J. Phys.: Condens. Matter* **28**, 275201 (2016).
38. W. Hofmann and W. Jäniche: Die Struktur von Aluminiumborid AlB2. *Z. Phys. Chem.* **31B**, 214 (1936).
39. M.L. Whittaker, H.Y. Sohn, and R.A. Cutler: Oxidation kinetics of aluminum diboride. *J. Solid State Chem.* **207**, 163 (2013).

https://doi.org/10.1557/jmr.2018.173 Published online by Cambridge University Press